GEOPHYSICS, VOL. 86, NO. 5 (SEPTEMBER-OCTOBER 2021); P. WC1–WC9, 7 FIGS.
10.1190/GEO2020-0867.1

DOI:10.1190/geo2020-0867.1

Marchenko multiple elimination and full-wavefield migration in a resonant pinch-out model

Evert Slob[1], Lele Zhang[2], and Eric Verschuur[3]

ABSTRACT

Marchenko multiple elimination schemes are able to attenuate all internal multiple reflections in acoustic reflection data. These can be implemented with and without compensation for two-way transmission effects in the resulting primary reflection data set. The methods are fully automated and run without human intervention, but they require the data to be properly sampled and preprocessed. Even when several primary reflections are invisible in the data because they are masked by overlapping multiples, such as in the resonant wedge model, all missing primary reflections are restored and recovered with the proper amplitudes. Investigating the amplitudes in the primary reflections after multiple elimination with and without compensation for transmission effects shows that transmission effects are properly accounted for in a constant-velocity model. When the layer thickness is one quarter of the wavelength at the dominant frequency of the source wavelet, the methods cease to work properly. Full-wavefield migration relies on a velocity model and runs a nonlinear inversion to obtain a reflectivity model, which results in the migration image. The primary reflections that are masked by interference with multiples in the resonant wedge model are not recovered. In this case, minimizing the data misfit function leads to the incorrect reflector model even though the data fit is optimal. This method has much lower demands on data sampling than the multiple elimination schemes, but it is prone to getting stuck in a local minimum even when the correct velocity model is available. A hybrid method that exploits the strengths of each of these methods could be worth investigating.

INTRODUCTION

Multiples can be regarded as a nuisance or as a source of information. In either case, being able to discriminate multiples from primaries plays an important role in making better subsurface images. Multiples can be seen as repetitive combinations of primaries that carry only information that is present in the primaries. Several studies aim to predict and remove them from the data (Weglein et al., 1997; Jakubowicz, 1998; ten Kroode, 2002; Berkhout and Verschuur, 2005; Liu et al., 2018). Apart from the method using the inverse-scattering series, these methods require some form of identification or model information and use adaptive subtraction. Multiples can be seen as helpful events that can fill in illumination gaps or improve the signal-to-noise ratio. Several studies aim to identify and use multiples in the imaging process (Whitmore et al., 2010; Verschuur and Berkhout, 2011; Zhang and Schuster, 2014; Wang et al., 2017; Guo and Schuster, 2018). The full-wavefield migration (FWM) method estimates reflectivity given a velocity model to explain all the data (Berkhout, 2014b; Davydenko and Verschuur, 2017) and has been applied to field data (Davydenko and Verschuur, 2018).

A new family of methods has been introduced based on Marchenko inverse scattering (Wapenaar et al., 2013). Many different approaches to data-driven redatuming and imaging without artifacts from multiples were derived and tested on synthetic and field data. Overburden removal (van der Neut and Wapenaar, 2016) led to different kinds of Marchenko multiple elimination (MME) schemes. The first kind uses either "double focusing" (Staring and Wapenaar, 2020), which includes source-receiver redatuming or "double dereverberations" (Staring et al., 2021), with the sources and receivers

Manuscript received by the Editor 30 November 2020; revised manuscript received 17 February 2021; published ahead of production 20 April 2021; published online 07 July 2021.
[1]Delft University of Technology, Department of Geoscience and Engineering, Stevinweg 1, Delft 2626 CN, The Netherlands. E-mail: e.c.slob@tudelft.nl.
[2]Delft University of Technology, Department of Geoscience and Engineering, Stevinweg 1, Delft 2626 CN, The Netherlands and Delft University of Technology, Delphi Consortium, Mekelweg 5, Delft 2628 CD, The Netherlands. E-mail: L.Zhang-1@tudelft.nl (corresponding author).
[3]Delft University of Technology, Delphi Consortium, Mekelweg 5, Delft 2628 CD, The Netherlands. E-mail: d.j.verschuur@tudelft.nl.

DOI:10.1190/geo2020-0867.1

kept at the acquisition surface. The schemes are implemented with adaptive subtraction, use offset-dependent time truncations, and select a target primary reflection from the reflection response. In this way, internal multiples limited to occurring only in the overburden are attenuated, whereas other multiples, such as multiples between the overburden and the medium below the target reflection, stay in the data. The second kind uses an offset-independent time truncation, does not require model information or adaptive subtraction, and attenuates all multiples. They are implemented without (Zhang and Staring, 2018) or with (Zhang et al., 2019b) compensation for transmission effects. These are called MME schemes or T-MME schemes with compensation for transmission effects. MME and T-MME schemes use the reflection response to act as a filter on itself without needing other information than the source-time signature. In principle, the outcome is a data set that contains primary reflections only, which forms an ideal input for migration schemes that assume primary-only data. The predicted multiples are obtained as an additional data set that can be used when desired to fill in illumination gaps, further improve the signal-to-noise ratio, make up for a missing primary, or any other reason the user may have in mind. The methods can be seen as ways to separate primary reflections from multiples. Free surface and internal multiples can be eliminated when pressure and particle velocity data are available without any preprocessing on the data, with up-down decomposition, after deghosting and source wavelet deconvolution, or after full preprocessing such that only internal multiples need to be removed (Slob and Zhang, 2021).

Independent of how a method predicts multiples, all multiples are assumed to not overlap with the associated primary reflections. When two consecutive primary reflections, for example, from the top and bottom of a layer, overlap, that layer can be said to be thin. The first interbed multiple will overlap with the primary from the bottom. When the layer becomes even thinner, more overlap will ultimately lead to the inability to distinguish between two (or more) primary reflections and interbed multiples. At some point, model-driven, data-driven, or hybrid methods will all fail in the sense that multiples will not be predicted anymore and two overlapping primary reflections will be treated as a single primary with a more complicated time behavior. A simple single thin layer example was given and analyzed in Slob et al. (2014), and a method to push the limit to higher frequencies can be found in Elison et al. (2020). Verschuur (2019) presents an interesting thin-layer example using a pinching-out wedge model bounded at the top and bottom by two horizontal reflectors. Here, we investigate the performance of the MME scheme on a similar but resonant model. We look at the effect of different center frequencies of the source-time function on the ability of the scheme to separate primary reflections from multiples and use the primaries to compute migration images. We also perform FWM on the same data sets and compare the image results.

This paper is organized as follows. After the introduction, we briefly outline the MME scheme. We then show the model and numerical results of multiple elimination for three different bandwidths and investigate the effects of the thinning layers under different angles. We show the amplitude behavior of the reflections from the bottom reflector in the zero-offset section and compare with the expected amplitude. We then show the images that are obtained from the data sets after multiple elimination and compare with the images made from the original data and after FWM. Finally, we discuss the performances of the multiple elimination and FWM schemes and highlight their limitations.

BRIEF REVIEW OF MME

In Marchenko redatuming, the receivers at the acquisition surface are redatumed to a chosen position inside the heterogeneous medium (Wapenaar et al., 2014a). This chosen position becomes a virtual receiver point, and the resulting field at that receiver is the corresponding virtual impulse response or Green's function with the sources unchanged in their original location. The up- and downgoing parts of this Green's function are used to create images without artifacts from multiple reflections. This has become known as Marchenko imaging (Wapenaar et al., 2014b). The redatuming step requires the first arrival of the wavefield from the sources to the virtual receiver as a known input wavefield. Because this field is unknown, an estimate is used to compute the initial part of the downgoing focusing function. The required knowledge can be built; for example, with a macrovelocity model. Once this estimate is known, the Green's functions and the artifact-free subsurface image are obtained without requiring further model information.

The need to know the initial part of the downgoing focusing function was removed in van der Neut and Wapenaar (2016) to remove the effect of the overburden on the target reflections. This is done by propagating the initial downgoing parts of all focusing functions at a certain depth level back to one physical receiver at the acquisition surface. Keeping focus in a physical receiver location has two merits. The first is that the initial downgoing part of the projected focusing function is always a unit impulse in the horizontal position of the physical receiver and in time. It is no longer an unknown. The second is that the timing of all events in the resulting upgoing part of projected Green's function is the same as that of the data. Removing the effects of the overburden in this way is very similar to the 1D approaches of Goupillaud (1961) and Kunetz (1964). The difference is that they used a recursive scheme involving only convolutions, whereas the Marchenko method uses convolutions and correlations, which renders it a nonrecursive method (Slob et al., 2020). In three dimensions, the time truncations are a function of some two-way traveltime from a source to the former focusing level and back to the receiver. This step requires model information to determine the offset-dependent traveltimes.

The need for model information was removed in Zhang and Staring (2018) where offset-independent time truncations are used. The truncation time is then a free parameter that can be chosen as any desired output time of the scheme. At this point, the MME scheme is totally model-free. The former back-projected focusing functions are changed because of the choice of offset-independent truncation times. The primary reflections that are filtered out from the reflection response can be collected in a new data set, where they occur at their physical two-way traveltime and with their physical amplitude as they are recorded. This means that the primary reflections are filtered out from the modified back-projected Green's functions. This is the MME scheme.

The unknown parts of the up- and downgoing modified back-projected focusing functions are denoted as $h^{\pm}(\mathbf{x}_0', \mathbf{x}_0'', t, \tau)$ where the plus- and minus-signs indicate the down- and upgoing parts, respectively; the position vectors $\mathbf{x}_0'$ and $\mathbf{x}_0''$ represent the receiver and source locations, respectively; t is the time; and τ is the truncation

time. The functions are wavefields computed from the reflection response for $0 < t < \tau - \epsilon$, where ϵ is half the time duration of the source-time signature, as

$$h^-(\mathbf{x}_0', \mathbf{x}_0'', t, \tau) - \int_{\partial \mathbb{D}_0} R(\mathbf{x}_0', \mathbf{x}, t) * h^+(\mathbf{x}, \mathbf{x}_0'', t, \tau) \mathrm{d}\mathbf{x} = R(\mathbf{x}_0', \mathbf{x}_0'', t), \tag{1}$$

$$h^+(\mathbf{x}_0', \mathbf{x}_0'', t, \tau) - \int_{\partial \mathbb{D}_0} R(\mathbf{x}_0', \mathbf{x}, -t) * h^-(\mathbf{x}, \mathbf{x}_0'', t, \tau) \mathrm{d}\mathbf{x} = 0. \tag{2}$$

In these equations, $*$ indicates temporal convolution and $\mathbf{x}$ is the coordinate vector for all sources at the acquisition surface $\partial \mathbb{D}_0$. Once h^+ is known, we retrieve for each source-receiver pair the time sample for the primary reflection data set R_t as

$$R_t(\mathbf{x}_0', \mathbf{x}_0'', \tau) = R(\mathbf{x}_0', \mathbf{x}_0'', \tau) + \int_{\partial \mathbb{D}_0} [R(\mathbf{x}_0', \mathbf{x}, t) * h^+(\mathbf{x}, \mathbf{x}_0'', t, \tau)]_{t=\tau} \mathrm{d}\mathbf{x}, \tag{3}$$

which is the result from the MME scheme. The subscripted square bracketed expression in the integral means that, after the time convolution is evaluated, the result at $t = \tau$ is taken. A similar data set can be obtained by evaluating equations 1 and 2 for $0 < t < \tau + \epsilon$. In that case, the primary reflection is captured at $t = \tau$ by approaching the boundary from below, which means that the desired primary reflection event is present in h^-, and it is retrieved as

$$R_r(\mathbf{x}_0', \mathbf{x}_0'', \tau) = h^-(\mathbf{x}_0', \mathbf{x}_0'', \tau, \tau), \tag{4}$$

which is the result from the T-MME scheme (Zhang et al., 2019b). Details on the numerical implementation and numerical illustrations of the MME and T-MME schemes can be found in Thorbecke et al. (2021).

BRIEF REVIEW OF FWM

The one-way representation of seismic data, using a multidimensional version of the Bremmer series (Wapenaar, 1996), was introduced as a modeling engine as full-wavefield modeling (Berkhout, 2014a) in nonlinear imaging known as FWM (Berkhout, 2014b). We describe the method using the matrix notation of Davydenko and Verschuur (2017). At any depth level z_m, the waves that leave the level in a down- or upgoing direction are denoted $Q^{\pm}(z_m)$, whereas the waves that arrive at that depth level from above or below are denoted $P^{\pm}(z_m)$. The reflection operator at that level is denoted $R^{\cup}$ for waves from above and $R^{\cap}$ for waves from below. The waves that leave that level can be expressed in terms of the waves that arrive there and the reflections that occur at that level as

$$Q^{\pm}(z_m) = P^{\pm}(z_m) + R^{\cup}(z_m) P^{+}(z_m) + R^{\cap}(z_m) P^{-}(z_m), \tag{5}$$

which includes transmission effects across the boundary. In the second step, the wavefield $P^{\pm}(z_m)$ is extrapolated to the adjacent depth level according to

$$P^{\pm}(z_m) = W(z_m, z_{m\mp1}) Q^{\pm}(z_{m\mp1}), \tag{6}$$

where $W(z_m, z_{m\pm1})$ represents a one-way wavefield extrapolation operator toward the depth level z_m from the neighboring depth level $z_{m\pm1}$. Equation 6 describes a lateral convolution process in the space-frequency domain with a local explicit one-way propagator that depends on the (laterally varying) local velocity between depth levels $z_{m\mp1}$ and z_m. Such an operator can be calculated by the inverse spatial Fourier transform of a phase-shift operator (Gazdag, 1978), or via more advanced optimization techniques (Thorbecke et al., 2004). In theory, FWM can explain all of the data through this modeling procedure. When the model is known, the reflection operators can be constructed and one round trip is sufficient to model the data. In the inversion procedure, the model is not known and several round trips will be necessary to explain the data given a velocity model. The misfit between the modeled and the measured data is minimized through regularized least-squares inversion to find the best possible reflection operators and image. Details of the method can be found in Berkhout (2014b) and Davydenko and Verschuur (2017).

NUMERICAL RESULTS FROM A RESONANT WEDGE MODEL

We use a model with a constant velocity of 2000 m/s and two density values of 1000 and 2000 kg/m^3. This results in local reflection coefficients of $r = \pm 1/3$ at any reflector in the model. The model is a layered wedge embedded between two horizontal reflectors. The wedge has six layers with alternating density. Each layer has a thickness of 100 m in the left side of the model and a vanishing thickness in the right side of the model. All wedge layers have the same thickness in our model resulting in a resonant model, contrary to the model in Verschuur (2019). The density model is shown in Figure 1, where the dark- and light-gray colors represent values of $\rho = 1000$ kg/m^3 and $\rho = 2000$ kg/m^3, respectively. We model the reflection data with a 15, 30, and 45 Hz Ricker wavelet with 401 sources and receivers, each spaced at 10 m. To model the data, the finite-difference scheme grid step sizes are $dx = dz = 2$ m and $dt = 4$ ms. We show results of the MME and T-MME schemes and compare them with the reflection responses. Before we look

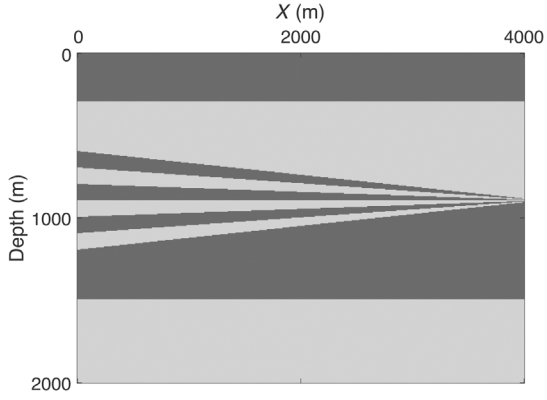

Figure 1. The density values as a function of horizontal location X (m) and depth (m). The dark- and light-gray colors represent values of $\rho = 1000$ kg/m^3 and $\rho = 2000$ kg/m^3, respectively.

at the results of the data panels before and after multiple elimination, it is good to understand that the grid creates a staircase approximation of the true dip of the boundary. Such staircases produce diffraction-like patterns in the data. These are brought out by eliminating multiples with the MME method and even more so with the T-MME method because the latter increases the amplitudes by correcting for transmission amplitude effects. This gives the panel a "noisier" appearance that should not be confused with inaccuracies of the method. In fact, we expect them to be more clearly visible after T-MME than after MME.

To create images before and after multiple elimination, we use one-way wave-equation migration with the correct velocity. FWM uses the same correct velocity to obtain the locations and values for reflectivity and produces an image as output. The FWM results are obtained with a subset of the data using shot spacing of 120 m and receiver spacing of 10 m. These images are compared with each other while overlaying the true model of Figure 1.

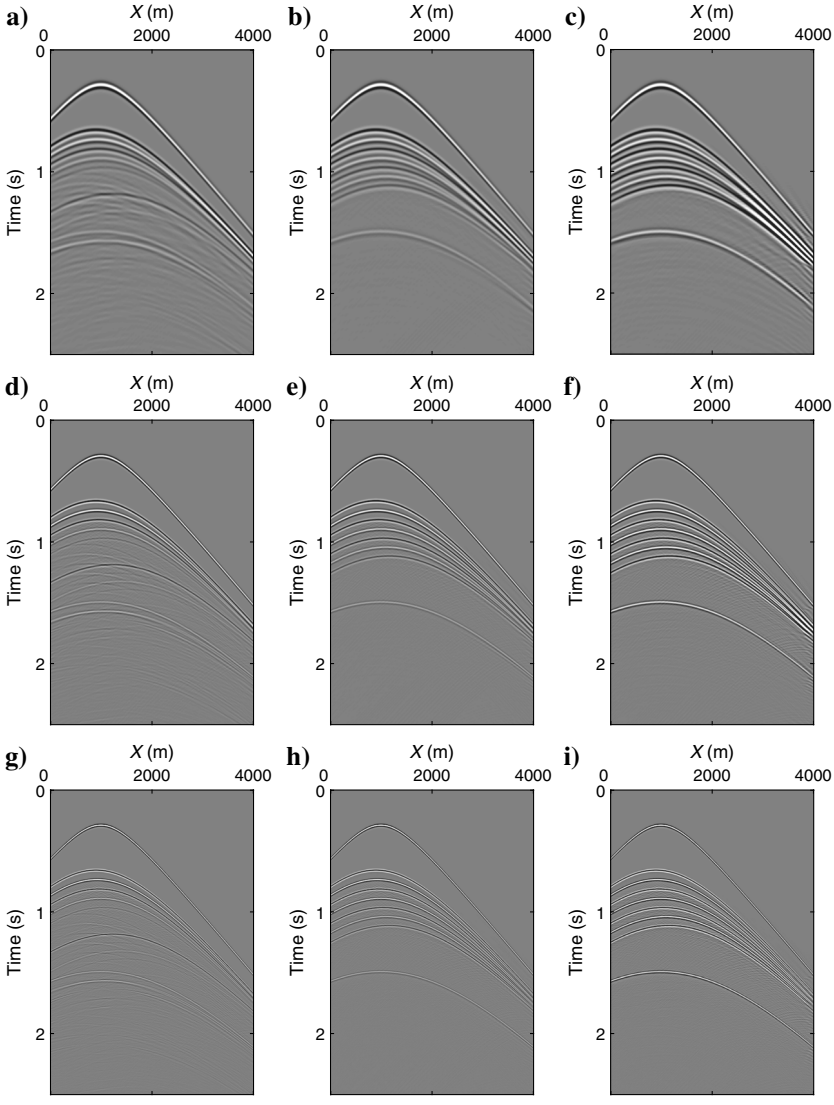

Figure 2. Reflection responses in input data, after MME, and after T-MME in (a-c) for the 15 Hz wavelet, in (d-f) for the 30 Hz wavelet, and in (g-i) for the 45 Hz wavelet.

Multiple elimination results

We show shot gathers for two different source positions. The first set of shot gathers is shown in Figure 2 for a shot location at $x = 1000$ m. The input data and the results after MME and T-MME are shown column-wise from left to right and for the 15, 30, and 45 Hz Ricker wavelets in rows from top to bottom. Three important observations can be made. First, many multiples are visible in the data shown in Figure 2a, 2d, and 2g. They seem to be almost completely eliminated after MME as shown in Figure 2b, 2e, and 2h and after T-MME as shown in Figure 2c, 2f, and 2i. After multiple elimination, the seven primary reflections from the reflectors in the wedge part of the model are clearly visible for receivers from 0 to 2000 m at 15 Hz (Figure 2b and 2c), to 3000 m at 30 Hz (Figure 2e and 2f) and in the whole panel at 45 Hz (Figure 2h and 2i).

The second observation is that the data panels do not show all reflections from the wedge. This can be seen by comparing Figure 2a, 2d, and 2g with Figure 2b, 2e, and 2h. The multiples mask the primary reflections from the bottom two reflectors in the wedge. MME and T-MME restore all primary reflections from the wedge and remove the multiple reflections as can be seen in Figure 2b and 2c, 2e and 2f, and 2h and 2i. To see this better, we magnify the part in which the primaries are masked in the data but are visible after MME and T-MME. Figure 3 shows a part of the shot gather for the 30 Hz Ricker wavelet from 0 to 2000 m distance and in time between 0.8 and 1.4 s. Figure 3a–3c shows the data, the result after MME, and after T-MME, respectively, all at the same absolute amplitude scale. The reflection that we see in the top of the panel with an apex near 1000 m distance is from the third reflector in the wedge. By comparing the plots, we observe that the bottom four reflection events in Figure 3b and 3c are primary reflections from the wedge reflectors that are much weaker or are entirely missing in the data in Figure 3a. The strong event in the data that has an apex at approximately 1.2 s is almost entirely removed after multiple removal. We can see that the reflection amplitudes after T-MME as shown in Figure 3c are stronger than those after MME as shown in Figure 3b. These differences arise from transmission effect compensation in the T-MME scheme. This makes the remnant amplitude from the multiple reflection with its apex at 1.2 s and the scattering hyperbolas from the staircasing effect of discretizing the dipping reflectors for the finite-difference time-domain modeling step better visible in Figure 3c than in Figure 3b. This does not mean that the quality of the removal of the multiple with apex at 1.2 s is better for MME than for T-MME.

The third observation from Figure 2 is that the results after MME and after T-MME differ in subtle but important aspects. This occurs especially where the primary reflections overlap to-

ward the pinching out of the layers in the wedge. This is visualized more clearly by magnifying the right side of the panels. The result is shown in Figure 4 for distances from 2500 to 4000 m and in times between 1.2 and 2.2 s. Figure 4a–4c shows the data, the result after MME, and after T-MME, respectively, all at the same absolute amplitude scale. Also here we see that all multiples have been removed or attenuated and diffraction hyperbolas stand out more after multiple elimination. The multiples that can be seen in Figure 4b indicated by arrows are still present, whereas they seem to have vanished in Figure 4c. To capture an event in the MME result, a smaller truncation time is used than when capturing the same event in T-MME. The reason is that all multiples that are generated by a primary reflection that arrives at the acquisition surface within the truncation time window of $0 < t < \tau - \epsilon$ in equations 1 and 2 and the window of $0 < t < \tau + \epsilon$ in equation 3 are eliminated. This causes more multiples to be eliminated or attenuated in the T-MME result than in the MME result. However, in Figure 4c an event seems present just before the arrival of the reflection from the bottom horizontal reflector in the model, as indicated by the arrow and that is not visible in Figure 4b. Finally, T-MME shows stronger data truncation effects than MME as can be seen by the strong artifacts that are present between 3700 and 4000 m after the first reflection event, after the last reflection from the wedge, and after the reflection from the bottom horizontal reflector. Two truncation effects play a role here. One is the end of aperture effects, and the other is time truncation effects to solve equations 1 and 2; see Thorbecke et al. (2021) for more details.

The second set of shot gathers that we look at is for a shot position of 3000 m. The shot position is closer to where the layers in the wedge are thin compared with the wavelength at the wavelet's center frequency. The data sets are shown in Figure 5. The input reflection data and the results after MME and after T-MME are shown column-wise from left to right and for the 15, 30, and 45 Hz Ricker wavelets in rows from top to bottom. The result at 15 Hz shown in Figure 5a shows multiples across the wedge and wedge multiples in interaction with the reflections from the top and bottom reflectors in the model. Figure 5b and 5c shows that the large-scale multiples are well attenuated and almost entirely removed. We cannot see the seven expected primary reflections from the reflectors in the wedge, but the gap visible in Figure 5a is reduced in Figure 5b and removed in Figure 5c. We can also see that the reflection from the bottom reflector does not look like a single reflection. It is clear that some multiple amplitude remains after MME and T-MME in case such thin layers are present in the model. This is an imprint of the complexity of the wavefield that passes through the thinning part of the wedge and is then incident on the bottom horizontal reflector in which it generates a reflection with the complexity of the incident wavefield. The persistence of short-period multiples below resolution limits creates effects on all later primary reflections.

At 30 Hz, the situation is improved, even though between 3000 and 4000 m the primary reflections in the MME and T-MME results are not separated from each other, they do not seem to create many problems with the elimination of multiples. Similar to the results for the shot at 1000 m, also here the 30 Hz results show a remnant multiple below the reflection from the last reflector in the wedge and also one just below the reflection from the bottom reflector as can be seen in Figure 5e. In the result after T-MME, these two multiple events have been almost completely eliminated as can be seen in Figure 5f. We see artifacts between 3700 and 4000 m below the last events from the wedge and below the bottom reflection. We also see an event just preceding the bottom reflection between 3200 and 4000 m. These artifacts are effects from the inability to separate the multiples and primaries in thin layers in the wedge.

At 45 Hz, the situation has improved further. MME is more capable of removing multiples than at 30 Hz as can be seen by comparing Figure 5e to Figure 5h where the remnant multiples visible at 30 Hz have been eliminated at 45 Hz and are only visible in the rightmost 500 m. In the T-MME results, we see that the artifacts following the primary reflections have increased in amplitude compared with the results at 30 Hz, but the spurious event just preceding the bottom reflection has been reduced. We can conclude that these events are due to the pinching out of the wedge — the effect of which is increasingly more confined to smaller parts at the right side of the model with increasing source frequencies. Hence, these artifacts arise from resolution problems.

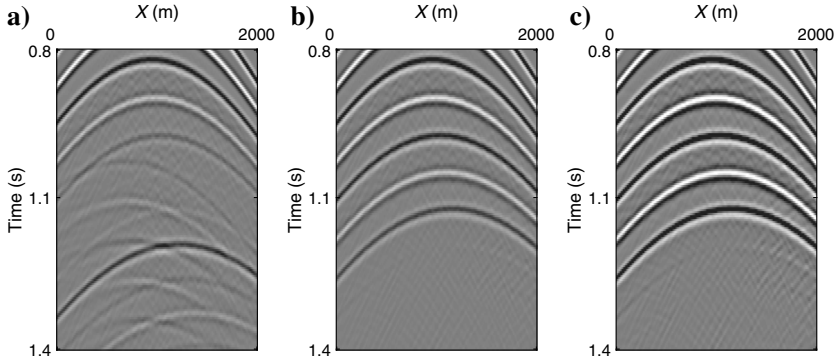

Figure 3. Magnified plots between 0 and 2000 m from 0.8 to 1.4 s for the 30 Hz Ricker wavelet in (a) the data, (b) after MME, and (c) after T-MME.

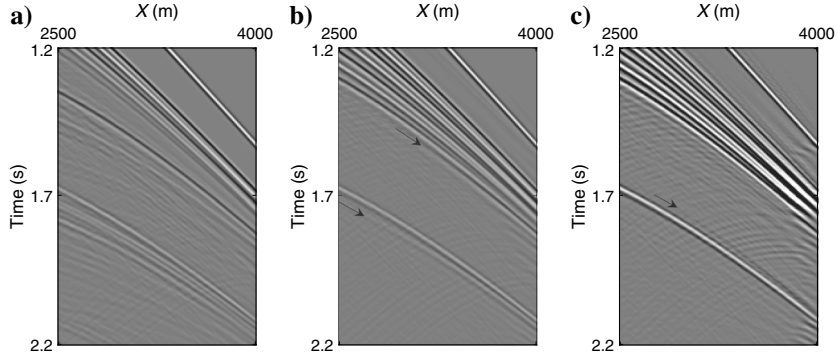

Figure 4. Magnified plots between 2500 and 4000 m from 1.2 to 2.2 s for the 30 Hz Ricker wavelet in (a) the data, (b) after MME, and (c) after T-MME.

MME is designed to remove all possible overlap from multiples, generated in the overburden, on a deeper primary reflection and aims to capture that primary reflection with its physical amplitude as recorded. Dynamically speaking, the primary reflection event itself is not touched by the method. This means that a deeper reflection after MME is expected to be a primary reflection with its physical amplitude including geometric spreading and transmission effects. T-MME is designed to do the same as MME and in addition to compensate for the two-way transmission effects of the waves that travel through the subsurface before they arrive again at the acquisition surface. The same event after T-MME is expected to be a primary reflection with its local reflection coefficient and geometric spreading only.

In our model, the ratio of the maximum amplitude of the reflection from the bottom reflector after MME and after T-MME should be position-independent. This ratio is equal to the two-way transmission effect for any offset. The passage from the source to the bottom reflector and back to the receivers traverses eight reflectors one way. Because the model has only density contrasts, each reflector has a reflection coefficient of $r = \pm 1/3$. The total two-way transmission effect is an amplitude multiplication factor of 0.390. We plot the ratios of the bottom reflection maximum amplitude in all zero-offset traces after MME and after T-MME in Figure 6 for data computed with the 15 Hz (the blue line) and 30 Hz (the red line) source wavelets together with the true two-way transmission effect (the green line). The dashed lines mark the horizontal distance of 450, 2700, 3000, and 3500 m, respectively. The ratio of the zero-offset trace amplitude at the arrival time of the bottom reflection event after MME and after T-MME for the 15 Hz wavelet data has an average of 0.394 between 500 and 2700 m. The first 450 m and last 500 m suffer from edge effects and between 2700 and 3500 m the resolution problems cause incomplete overburden multiple elimination and therefore amplitude inaccuracies in the ratio. At 15 Hz, the average error of the estimated transmission effect is just greater than 1%. To achieve the result shown for the 30 Hz wavelet, we had to model the data with shot and receiver spacing of 5 m, and we used $dx = dz = 1$ m but kept $dt = 4$ ms. We can see that the range at which the 30 Hz results is accurate is extended to 3000 m and with a slight increase in average error to 3500 m. For the modeled data with $dx = dz = 2$ m and 10 m shot and receiver spacing, the average error would rise to 4% at 30 Hz and after 3000 m the error would become very large, similar to what is shown in the graph.

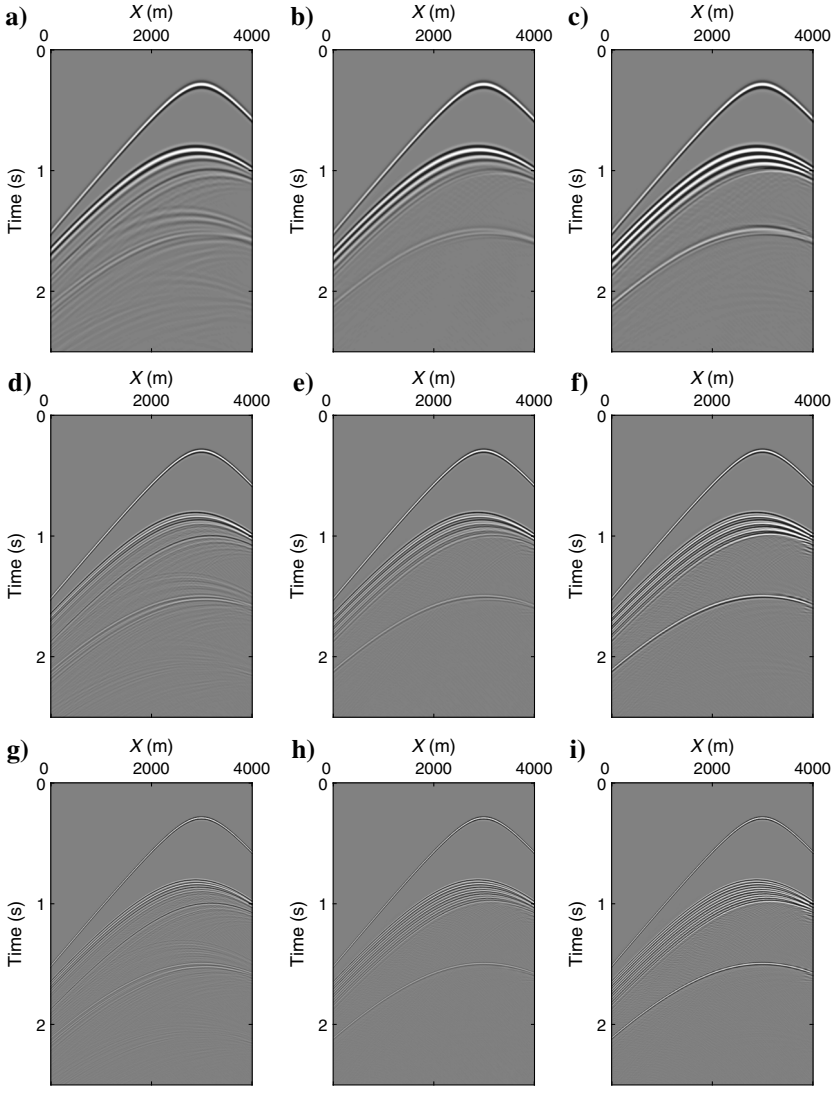

Figure 5. Reflection responses in the input data, after MME, and after T-MME in (a-c) for 15 Hz wavelet, in (d-f) for 30 Hz wavelet, and in (g-i) for 45 Hz wavelet.

Image results

The most challenging data set is with the 15 Hz Ricker wavelet. We therefore limit the image results section to images from those data sets but include FWM results. Figure 7 shows the images obtained from the data with the 15 Hz source wavelet overlaying the density model. The red and green colors in the background indicate 1000 and 2000 kg/m^3, respectively. Two dashed lines mark the horizontal positions of 2700 and 3000 m, respectively. Figure 7a–7d shows the image obtained from the modeled data, from the data after MME, after the FWM process, and from the data after T-MME, respectively. Recall that the layers in the wedge part have a 100 m thickness in the left and pinch out in the right. In Figure 7a, we can see that the reflections from the first two layers in the wedge do not suffer from interference and are properly imaged in the first 2700 m of the model. This approximately corresponds to a thickness that is one quarter of the wavelength at the center frequency. The bottom of the third reflector in the wedge is already much weaker, the bottom of the fourth reflector is almost absent, and the last two dipping reflectors are absent in the image. The weaker and absent reflectors are clearly visible in Figure 7b. From approximately 2700 m onward, the last two dipping reflectors are not visible in Figure 7b. Resolution limits prevent the elimination of multiples that fully mask the pri-

DOI:10.1190/geo2020-0867.1

mary reflections there, which are therefore not retrieved. Almost all ghost reflectors in the image, coming from multiple reflections that can be seen in Figure 7a, are not visible in the image in Figure 7b. One spurious reflector below the deepest dipping reflector is visible and another one just below the bottom reflector, indicated by arrows. The associated reflections were visible in the shot gathers, and they must be consistently present in all shot gathers to be imaged. Figure 7c shows that FWM is not able to remove the imprint of most multiples. However, it does reconstruct the missing reflectors, except for the top and bottom of the deepest dipping layer. Some parts of those reflectors are recovered, but just below the bottom of the wedge a new ghost reflector is present. This seems to suggest that FWM is able to build a reflectivity model when a primary reflection is masked by multiples, but in this extreme example not more than one primary is recovered. Figure 7d shows that T-MME produces a higher quality image than MME, in the sense that the spurious reflectors that were seen in the MME image have disappeared from the T-MME image. This suggests that the slightly better capability of T-MME to remove multiples near the resolution limit pays off in the image whereas the associated artifacts that we saw in the shot gathers do not end up visibly in the image. The images after MME and after T-MME show some spurious reflectors between 3000 and 4000 m below the wedge, where the layer thickness in the wedge is 25 m or less. These are indicated by ovals. It can be seen that these artifacts are stronger in the MME image than in the T-MME image.

DISCUSSION

The model that we use here can be considered a challenging model, even though it is a constant velocity model. It is challenging because the structure of the wedge part of the model results in primary reflections being masked by multiple reflections to the extent that no events show up in the data. The MME and T-MME schemes seem to be effective multiple elimination schemes. They remove the multiple reflections even when they fully overlap primary reflections and bring out the masked primary reflections. In the thinning part of the layers in the wedge when the thickness of each layer is less than one quarter of the wavelength at the center frequency of the wavelet, multiple elimination fails and remnant multiple events remain the data that lead to spurious reflectors in the image. T-MME performs better than MME when it comes to the removal of multiple reflections near the resolution limit. This comes with the generation of stronger artifacts. These artifacts occur for a limited number of source-receiver combinations and do not lead to artifacts in the T-MME image for the model used here. In the constant-velocity model used here, T-MME corrects for two-way transmission effects to high accuracy in the data with 15 and 30 Hz Ricker wavelets. The important downside of MME and T-MME, or any fully data-driven method, is that they require fine sampling that should satisfy the sampling criterion in space and time. In addition, the current model with constant velocity does not bring certain limitations that are inherent to the methods, such as turning waves or refractions and possible forward scattering that involves downward reflection followed by a down-up reflection. Such events are assumed to be absent in the processing of the data with the methods; see Zhang et al. (2019a) for more details. Figure 6 shows that the amplitude of the bottom reflector is recovered with reasonable accuracy at 30 Hz when the shot and receiver spacing was half of that for the 15 Hz wavelet. Numerical tests have shown that accuracy of the T-MME result depends on the shot and receiver spacing. The

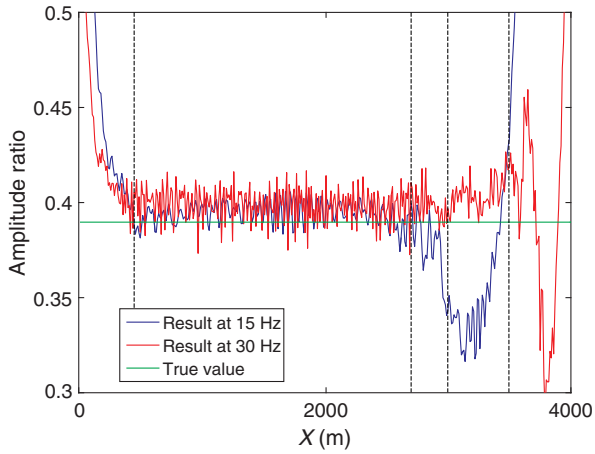

Figure 6. Maximum amplitude ratio of the bottom reflection event of the zero-offset traces after MME and after T-MME for 15 Hz (the blue line), 30 Hz (the red line) source wavelets, and the true two-way transmission effect (the green line); the dashed lines mark horizontal locations of 450, 2700, 3000, and 3700 m, respectively.

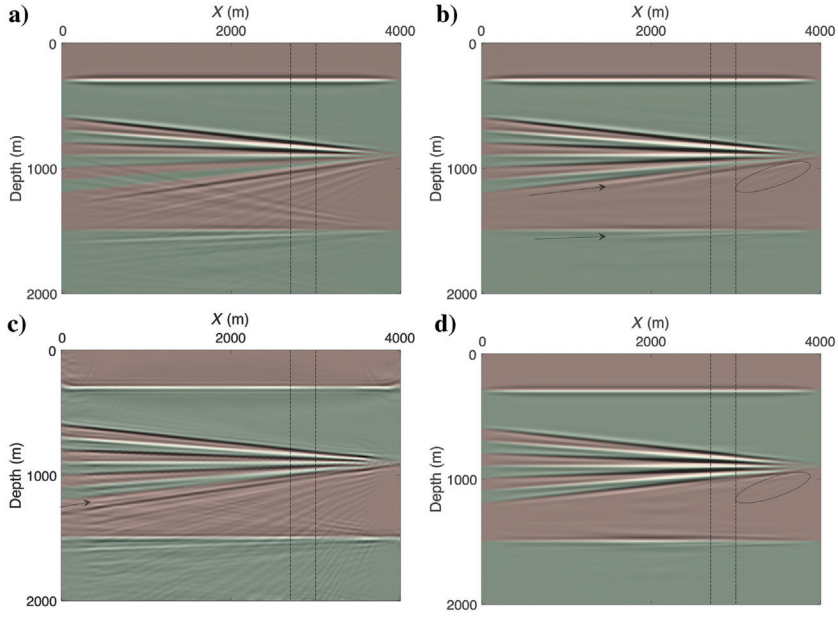

Figure 7. Images overlaying the density model: The gray and yellow colors in the background represent 1000 and 2000 kg/m^3, respectively; images are from (a) the data, (b) after MME, (c) FWM, and (d) after T-MME; all based on the data with the 15 Hz Ricker wavelet; dashed lines mark the horizontal locations of 2700 and 3000 m, respectively; arrows indicate spurious reflectors in the image after MME; and the ovals mark a few spurious reflectors.

DOI:10.1190/geo2020-0867.1

data should not be aliased, after which a denser data set can be obtained by exact interpolation within the bandwidth of the data. Missing far offsets is not detrimental, but missing near offsets can be harmful depending on the depth of the first reflector. In general, it is safe to say that the near-offset data should be filled in for MME or T-MME to work well. More information can be found in Staring and Wapenaar (2020) in the context of double focusing in 3D.

FWM requires a velocity model to make updates in the reflection operator at every depth level. These updates are obtained through a nonlinear inversion procedure by iterative forward modeling (Davydenko and Verschuur, 2017). In that sense, it can be seen as a model-driven method, although the image is iteratively derived from the data. If FWM would work as expected from theory, it would find the correct reflectivity model and the image would be the same as the T-MME image in the sense that all reflectors would have the same strength in the image. FWM does not achieve this in this extreme model. The visible difference toward the sides of the image compared with the other three images is the different treatment of the limited aperture of the data in FWM. The main reason why FWM cannot find the correct image is because in the end it solves a nonlinear inversion problem with the data misfit as a value to minimize and that is prone to local minima. With this resonant subsurface model, the inversion scheme is pushed directly into a local minimum, where the "fake" reflectors — events generated by strong periodic interference — are considered true reflectors and the inversion scheme will adjust the rest of the image such that the seismic data misfit is minimized. The fact that this solution indeed is a local minimum has been validated by applying FWM with a strong constraint on the true reflector locations, which ended up in a slightly lower L2 data misfit (2.57% versus 2.70%). However, the inversion process does improve vertical resolution and lateral illumination because this is required to fit the data. Note that in the case of a nonresonant version of this model, as shown by Verschuur (2019), FWM could avoid this local minimum and find a more reliable image. Finally, it should also be mentioned that the FWM results shown here are obtained with a shot spacing six times larger than used for MME and T-MME. It will be interesting to investigate whether a hybrid data-model driven method could exploit the strength of MME or T-MME to remove multiple reflections and combine the ability of FWM to model sparsely sampled data sets. A possible and potentially interesting combination is to investigate aliased data to use the modeling capability of FWM to fill in the necessary shots and receiver positions for MME to work and use the quality of the MME results to improve the velocity model for FWM. If in addition T-MME is used, we could also make the two methods work together to not only update the velocity model but also improve the reflectivity of the model. This could start with an iteration of FWM to fill in the necessary shot and receiver positions and perform one T-MME iteration to predict multiples. The prediction can be evaluated for amplitude errors and timing errors. This may be beneficial for the next iteration of FWM to update the velocity model and reflectivity to improve the filling of shot and receiver positions. This can be followed with a new first T-MME iteration to predict the multiples. When the prediction matches all events in time, the next MME iteration can be done. No new multiples will be predicted, but all of the amplitudes should be improved. This can lead to the next FWM iteration to improve the reflectivity model. This iteration process can be continued until MME can remove all multiples and FWM produces an artifact-free image and a correct reflectivity model.

CONCLUSION

We have shown that MME and T-MME remove multiple reflections and can recover primary reflections that are invisible in the data in case they are canceled due to interference with multiple reflections. We have shown that T-MME correctly removes the two-way transmission effects in a constant velocity model. When layers are one quarter of the wavelength at the center frequency of the source wavelet or less, multiple elimination ceases to work and remnant multiple reflections remain in the data in a coherent way. As a consequence, they are then imaged as spurious reflectors. Waves traveling through layers with a thickness less than one quarter of the wavelength at the center frequency become more complicated than the MME and T-MME methods assume. This more complicated wavefield leaves an imprint on reflections from deeper targets that is not removed by MME or T-MME. This imprint becomes visible in the image of these deeper reflectors. In such situations, compensation for transmission effects fails as well. Because these schemes are fully data driven, they require the data to be properly sampled. In extreme cases such as shown in our example with FWM, model-driven schemes may not recover more than one invisible primary reflection. The data misfit is well-minimized with an incorrect reflector model clearly showing the effect of a local minimum in the solution space. The fact that FWM can work with sparser data than (T-)MME suggests that investigating combining the strengths of the two methods can be useful.

ACKNOWLEDGEMENTS

The authors thank the sponsors of the Delphi Consortium for their support.

DATA AND MATERIALS AVAILABILITY

Data associated with this research are available and can be obtained by contacting the corresponding author.

REFERENCES

Berkhout, A. J., 2014a, Review paper: An outlook on the future of seismic imaging — Part 1: Forward and reverse modelling: Geophysical Prospecting, **62**, 911–930, doi: 10.1111/1365-2478.12161.

Berkhout, A. J., 2014b, Review paper: An outlook on the future of seismic imaging — Part 2: Full-wavefield migration: Geophysical Prospecting, **62**, 931–949, doi: 10.1111/1365-2478.12154.

Berkhout, A. J., and D. J. Verschuur, 2005, Removal of internal multiples with the common focus-point (CFP) approach — Part 1: Explanation of the theory: Geophysics, **70**, no. 3, V45–V60, doi: 10.1190/1.1925753.

Davydenko, M., and D. J. Verschuur, 2017, Full-wavefield migration: Using surface and internal multiples in imaging: Geophysical Prospecting, **65**, 7–21, doi: 10.1111/1365-2478.12360.

Davydenko, M., and D. J. Verschuur, 2018, Including and using internal multiples in closed-loop imaging — Field data examples: Geophysics, **83**, no. 4, R297–R305, doi: 10.1190/geo2017-0533.1.

Elison, P., M. S. Dukalski, K. de Vos, D. J. van Manen, and J. O. A. Robertsson, 2020, Data-driven control over short-period internal multiples in media with a horizontally layered overburden: Geophysical Journal International, **221**, 769–787, doi: 10.1093/gji/ggaa020.

Gazdag, J., 1978, Wave equation migration with the phase-shift method: Geophysics, **43**, 1342–1351, doi: 10.1190/1.1440899.

Goupillaud, P. L., 1961, An approach to inverse filtering of near surface effects from seismic records: Geophysics, **26**, 754–760, doi: 10.1190/1.1438951.

Guo, B., and G. T. Schuster, 2018, Superresolution imaging using resonant multiples: Geophysics, **83**, no. 2, A23–A28, doi: 10.1190/geo2017-0311.1.

Jakubowicz, H., 1998, Wave equation prediction and removal of interbed multiples: 68th Annual International Meeting, SEG, Expanded Abstracts, 1527–1530, doi: 10.1190/1.1820204.

Kunetz, G., 1964, Généralisation des opérateurs d'anti-resonance a un nombre quelconque de réflecteurs: Geophysical Prospecting, **12**, 283–289, doi: 10.1111/j.1365-2478.1964.tb01904.x.

Liu, J. H., T. Y. Hu, and G. X. Peng, 2018, Suppressing seismic inter-bed multiples with the adaptive virtual events method: Chinese Journal of Geophysics-Chinese Edition, **61**, 1196–1210, doi: 10.6038/cjg2018L0663.

Slob, E., K. Wapenaar, F. Broggini, and R. Snieder, 2014, Seismic reflector imaging using internal multiples with Marchenko-type equations: Geophysics, **79**, no. 2, S63–S76, doi: 10.1190/geo2013-0095.1.

Slob, E., K. Wapenaar, and S. Treitel, 2020, Tutorial: Unified 1D inversion of the acoustic reflection response: Geophysical Prospecting, **68**, 1425–1442, doi: 10.1111/1365-2478.12946.

Slob, E., and L. Zhang, 2021, Unified elimination of 1D acoustic multiple reflections: Geophysical Prospecting, **69**, 327–348, doi: 10.1111/1365-2478.13057.

Staring, M., M. Dukalski, M. Belonosov, R. Baardman, J. Yoo, R. Hegge, R. van Borselen, and K. Wapenaar, 2021, R-EPSI and Marchenko equation-based workflow for multiple suppression in the case of a shallow water layer and a complex overburden: A 2D case study in the Arabian Gulf: Geophysics, **86**, no. 2, Q15–Q25, doi: 10.1190/geo2020-0204.1.

Staring, M., and K. Wapenaar, 2020, Three-dimensional Marchenko internal multiple attenuation on narrow azimuth streamer data of the Santos Basin, Brazil: Geophysical Prospecting, **68**, 1864–1877, doi: 10.1111/1365-2478.12964.

ten Kroode, F., 2002, Prediction of internal multiples: Wave Motion, **35**, 315–338, doi: 10.1016/S0165-2125(01)00109-3.

Thorbecke, J., K. Wapenaar, and G. Swinnen, 2004, Design of one-way wavefield extrapolation operators, using smooth functions in WLSQ optimization: Geophysics, **69**, 1037–1045, doi: 10.1190/1.1778246.

Thorbecke, J., L. Zhang, K. Wapenaar, and E. Slob, 2021, Implementation of the Marchenko multiple elimination algorithm: Geophysics, **86**, no. 2, F9–F23, doi: 10.1190/geo2020-0196.1.

van der Neut, J., and K. Wapenaar, 2016, Adaptive overburden elimination with the multidimensional Marchenko equation: Geophysics, **81**, no. 5, T265–T284, doi: 10.1190/geo2016-0024.1.

Verschuur, D. J., and A. J. Berkhout, 2011, Seismic migration of blended shot records with surface-related multiple scattering: Geophysics, **76**, no. 1, A7–A13, doi: 10.1190/1.3521658.

Verschuur, E., 2019, Imaging including internal multiples: Influence of broadband acquisition: 81st Annual International Conference and Exhibition, EAGE, Extended Abstracts, WS08–WS14, doi: 10.3997/2214-4609.201901957.

Wang, Y., Y. Zheng, Q. Xue, X. Chang, T. W. Fei, and Y. Luo, 2017, Reverse time migration of multiples: Reducing migration artifacts using the wavefield decomposition imaging condition: Geophysics, **82**, no. 4, S307–S314, doi: 10.1190/geo2016-0354.1.

Wapenaar, C. P. A., 1996, One-way representations of seismic data: Geophysical Journal International, **127**, 178–188, doi: 10.1111/j.1365-246X.1996.tb01543.x.

Wapenaar, K., F. Broggini, E. Slob, and R. Snieder, 2013, Three-dimensional single-sided Marchenko inverse scattering, data-driven focusing, Green's function retrieval, and their mutual relations: Physical Review Letters, **110**, 084301, doi: 10.1103/PhysRevLett.110.084301.

Wapenaar, K., J. Thorbecke, J. van der Neut, F. Broggini, E. Slob, and R. Snieder, 2014a, Green's function retrieval from reflection data, in absence of a receiver at the virtual source position: Journal of the Acoustical Society of America, **135**, 2847–2861, doi: 10.1121/1.4869083.

Wapenaar, K., J. Thorbecke, J. van der Neut, F. Broggini, E. Slob, and R. Snieder, 2014b, Marchenko imaging: Geophysics, **79**, no. 3, WA39–WA57, doi: 10.1190/geo2013-0302.1.

Weglein, A. B., F. A. Gasparotto, P. M. Carvalho, and R. H. Stolt, 1997, An inverse scattering series method for attenuating multiples in seismic reflection data: Geophysics, **62**, 1975–1989, doi: 10.1190/1.1444298.

Whitmore, N. D., A. A. Valenciano, and W. Sollner, 2010, Imaging of primaries and multiples using a dual-sensor towed streamer: 80th Annual International Meeting, SEG, Expanded Abstracts, 3187–3192, doi: 10.1190/1.3513508.

Zhang, D., and G. T. Schuster, 2014, Least-squares reverse time migration of multiples: Geophysics, **79**, no. 1, S11–S21, doi: 10.1190/geo2013-0156.1.

Zhang, L., and M. Staring, 2018, Marchenko scheme based internal multiple reflection elimination in acoustic wavefield: Journal of Applied Geophysics, **159**, 429–433, doi: 10.1016/j.jappgeo.2018.09.024.

Zhang, L., J. Thorbecke, K. Wapenaar, and E. Slob, 2019a, Data-driven internal multiple elimination and its consequences for imaging: A comparison of strategies: Geophysics, **84**, no. 5, S365–S372, doi: 10.1190/geo2018-0817.1.

Zhang, L., J. Thorbecke, K. Wapenaar, and E. Slob, 2019b, Transmission compensated primary reflection retrieval in the data domain and consequences for imaging: Geophysics, **84**, no. 4, Q27–Q36, doi: 10.1190/geo2018-0340.1.

Biographies and photographs of the authors are not available.

DOI:10.1190/geo2020-0867.1